POLITECNICO DI TORINO
Repository ISTITUZIONALE

A shallow-water theory of river bedforms in supercritical conditions

*Original*
A shallow-water theory of river bedforms in supercritical conditions / Vesipa, R., Camporeale, C.V., Ridolfi, L.. - In: PHYSICS OF FLUIDS. - ISSN 1070-6631. - STAMPA. - 24:9(2012), pp. 094104-1-094104-15. [10.1063/1.4753943]

*Availability:*
This version is available at: 11583/2502542 since:

*Publisher:*
American Institute of Physics

*Published*
DOI:10.1063/1.4753943

*Terms of use:*

This article is made available under terms and conditions as specified in the corresponding bibliographic description in the repository

*Publisher copyright*

(Article begins on next page)

13 June 2026

AIP | Physics of Fluids

# A shallow-water theory of river bedforms in supercritical conditions

Riccardo Vesipa, Carlo Camporeale, and Luca Ridolfi

Citation: Phys. Fluids **24**, 094104 (2012); doi: 10.1063/1.4753943

View online: http://dx.doi.org/10.1063/1.4753943

View Table of Contents: http://pof.aip.org/resource/1/PHFLE6/v24/i9

Published by the American Institute of Physics.

---

## Related Articles

Instability in evaporative binary mixtures. II. The effect of Rayleigh convection
Phys. Fluids 24, 094102 (2012)

Asymptotics and numerics of a family of two-dimensional generalized surface quasi-geostrophic equations
Phys. Fluids 24, 095101 (2012)

Regular and chaotic dynamics of a fountain in a stratified fluid
Chaos 22, 023116 (2012)

Pattern formation in a reaction-diffusion-advection system with wave instability
Chaos 22, 023112 (2012)

Scaling percolation in thin porous layers
Phys. Fluids 23, 122107 (2011)

---

## Additional information on Phys. Fluids

Journal Homepage: http://pof.aip.org/

Journal Information: http://pof.aip.org/about/about_the_journal

Top downloads: http://pof.aip.org/features/most_downloaded

Information for Authors: http://pof.aip.org/authors

ADVERTISEMENT

Downloaded 21 Sep 2012 to 130.192.58.87. Redistribution subject to AIP license or copyright; see http://pof.aip.org/about/rights_and_permissions

PHYSICS OF FLUIDS **24**, 094104 (2012)

# A shallow-water theory of river bedforms in supercritical conditions

Riccardo Vesipa, Carlo Camporeale, and Luca Ridolfi
*Department of Environmental, Land and Infrastructure Engineering,*
*Politecnico di Torino, C. so Duca degli Abruzzi 24, 10129 Torino, Italy*

(Received 27 April 2012; accepted 8 August 2012; published online 19 September 2012)

A supercritical free-surface turbulent stream flowing over an erodible bottom can generate a characteristic pattern of upstream migrating bedforms known as antidunes. This morphological instability, which is quite common in fluvial environments, has attracted speculative and applicative interests, and has always been modelled in 2D or 3D mathematical frameworks. However, in this work we demonstrate that antidune instability can be described by means of a suitable one-dimensional model that couples the Dressler equations to a mechanistic model of the sediment particle deposition/entrainment. The results of the linear stability analysis match the experimental data very well, both for the instability region and the dominant wavelength. The analytical tractability of the 1D modeling allows us (1) to elucidate the key physical processes which drive antidune instability, (2) to show the secondary role played by sediment inertia, (3) to obtain the dispersion relation in explicit form, and (4) to demonstrate the absolute nature of antidune instability. © *2012 American Institute of Physics*. [http://dx.doi.org/10.1063/1.4753943]

## I. INTRODUCTION

Over the last 50 years, remarkable efforts have been devoted to the study of the morphological dynamics of alluvial rivers, in which a turbulent free-surface stream interacts with a cohesionless bottom. River morphodynamics have in fact posed a formidable variety of theoretical questions concerning the nature of sediment-fluid interactions[1] and is still stimulating the fluid dynamics community to investigate several open issues, such as non-modal analysis,[2,3] the convective/absolute nature of instabilities,[4,5] the occurrence of bedforms under laminar conditions,[6] and the significance of 3D effects.[7] Apart from speculative reasons, the interest in this topic lies in the impact of bedforms on human activities and environment preservation. Bedforms interfere with navigation,[8,9] and fluvial infrastructures,[10] are important paleo-climatic proxies,[11–13] and they also affect a number of key bio-geochemical processes that occur in river corridors.[14–16]

In this paper, focus is on the micro-scale bedforms that are generated by supercritical streams, i.e., when the Froude number is greater than one. These bedforms are traditionally called *antidunes*. They are characterized by a periodic pattern that migrates upstream and induces the free surface to be in-phase with the bottom (Fig. 1). Antidunes have always been investigated in a two-dimensional mathematical framework, while the linear stability of the fully 3D problem has only recently been proposed.[7] Therefore, it is commonly assumed that the simplest hydrodynamic model that is able to predict antidunes has to be at least two-dimensional. Such a conjecture is motivated by evidence that bedform amplitude usually scales with the stream depth and, therefore, the vertical velocity and the non-hydrostatic component of pressure are assumed non-negligible. The main aim of the present work is to show that antidune instability can instead be correctly described by means of an appropriate one-dimensional depth-averaged model.

In the past, the fluid dynamics of a stream over antidunes were modelled using either irrotational or rotational 2D models. Basically, irrotational models assume that the evolution of an erodible bed depends on the flow velocity at the bottom and on an *ad hoc* phase-lag between the flow field and bed topography,[17–19] the latter being introduced in order to take into account those processes that

Downloaded 21 Sep 2012 to 130.192.58.87. Redistribution subject to AIP license or copyright; see http://pof.aip.org/about/rights_and_permissions

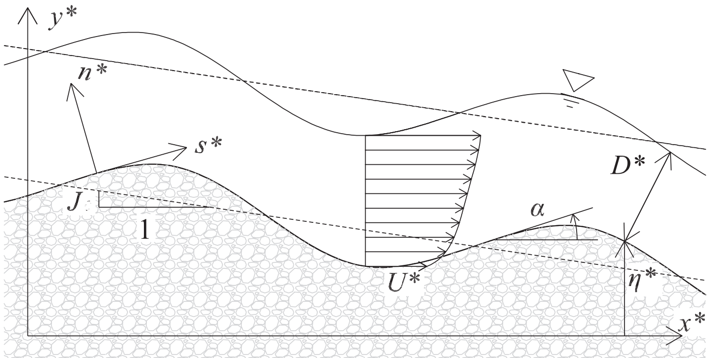

FIG. 1. Sketch of the physical problem. The dotted and continuous lines refer to unperturbed and antidune-like perturbed conditions, respectively.

are not described by the potential flow (e.g., flow separation). However, the evaluation of the right phase-lag continued to remain an open question until potential models were completely abandoned after the artificiality of the introduction of the phase lag was demonstrated by Coleman.[20] Rotational models allowed important improvements in the antidune modelling. The first attempts adopted the vorticity equation with a constant eddy viscosity.[21,22] However, a suspended load was necessary for the antidunes to occur, although several experiments demonstrated that a bedload alone is actually sufficient. Colombini[7,23] has recently proposed a more refined antidune model that couples a mixing length approach with the classical Meyer-Peter-Müeller (MPM) formulation of the bedload. The key point of this model is that it evaluates the shear stress that is responsible for the sediment transport at the top of the bed-load saltation layer. This leads to the correct prediction of antidunes considering the only bed-load.

In this paper, we propose a novel theory for antidunes, which is obtained by coupling 1D shallow-water equations with a mechanistic sediment transport formulation. We demonstrate that despite some simplifications in the modelling, the physical mechanisms required for the inception of the instability and for the correct selection of the dominant wavelength are preserved. Furthermore, the formulation of an analytically tractable theory allows us to obtain the dispersion relation in an explicit way. This important finding opens the way to further theoretical analyses on antidunes, concerning, for example, non-parallelism effects[24] or the absolute/convective nature of instability.[25] Such analyses in fact require sophisticated techniques that are precluded due to the mathematical complexity of the two-dimensional approaches used so far. In this paper, we will in particular demonstrate the absolute nature of antidune instability.

To the authors' knowledge, no depth-averaged flow model, coupled with any bottom evolution, has been able to detect antidune instability.[26] Di Cristo *et al.*[27] have recently proposed a morphodynamical model that couples the de Saint-Venant (dSV) shallow water equations with a modified MPM formula, and which takes into account sediment particle inertia. The bottom was found to be unstable in the supercritical regime, but the theory failed to correctly evaluate the marginal stability curves, thus any comparison with real data from measurements was hampered. Our model instead shows that two factors play a crucial role in the 1D modelling of antidune instability. The first factor concerns the non-hydrostatic component of the pressure distribution induced by bed curvature and its effect on the shear stresses. In order to describe this aspect, we adopt the flow modelling given by Dressler.[28] The second key point concerns sediment transport. In previous works, it was always modelled with empirical formulas derived from experiments in uniform equilibrium conditions (e.g., the MPM formula), that is, it is assumed that the particle deposition equals the entrainment at any point of the bed. However, this is an approximation in unstable conditions, the stream-bed system being far from the local equilibrium. For this reason, we do not assume any equilibrium conditions and instead adopt a mechanistic approach that is based on the the momentum exchange between the fluid and the sediment and on the (space- and time-dependent) balance of the forces acting on the sediment particles.[29,30] Such an approach allows the sediment transport rate to be modelled in terms

Downloaded 21 Sep 2012 to 130.192.58.87. Redistribution subject to AIP license or copyright; see http://pof.aip.org/about/rights_and_permissions

of particle velocity and areal concentration of the moving particles, and the bed evolution results from the competition between the local entrainment and deposition processes.

## II. MODELLING ASPECTS

Let us consider a turbulent open-channel flow over an undulated bed (see Figure 1) in which $\{x^*, y^*\}$ and $\{s^*, n^*\}$ are the (global) Cartesian and the (local) boundary-fitted reference systems, respectively. Henceforth, the asterisk refers to dimensional quantities. The bottom is defined by the equation $y^* - \eta^*(x) = 0$, where the function $\eta^*(x)$ is assumed to be continuous up to its third derivative. The uniform unperturbed condition—referred to with the subscript "0"—features a flat bed inclined with a constant slope $J$ and a depth equal to $D_0^*$.

According to Dressler,[28] we introduce the channel shallowness, $\sigma = (D^*/L^*)^2$ – $L^*$ being the longitudinal length scale of the problem—and consider the mass and momentum conservation equations for a two-dimensional irrotational flow written in curvilinear coordinates, flanked by suitable kinematic and dynamic conditions at the free surface as well as impermeability and non-slip conditions at the bottom. After expanding in term of $\sigma$ - a suitable approach being $\sigma = \mathcal{O}(10^{-2})$ in the antidune problem here considered—and using $D_0^*$ and $U_0^*$ to make the equations dimensionless (with $U_0^*$ the unperturbed flow velocity close to the bottom), Dressler obtained, from the kinematic condition at the order $\mathcal{O}(\sigma^0)$, the normal profile of the longitudinal velocity $\mathcal{U}(s, n, t) = U/\mathcal{C}$, where $\mathcal{C} = 1 - \kappa n$, $\kappa$ is the local bed curvature and $U(s, t) = \mathcal{U}|_{n=0}$ is the tangential velocity at the bottom, which is still unknown. The continuity and vertical momentum equations, at $\mathcal{O}(\sigma^1)$, instead provide the vertical profiles of the dimensionless normal velocity, $\mathcal{V}(s, n, t)$, and pressure $\mathcal{P}(s, n, t)$, respectively,

$$\mathcal{V} = \frac{\log \mathcal{C}}{\kappa \mathcal{C}} \frac{\partial U}{\partial s} - \frac{\partial \kappa}{\partial s}\left[\frac{n}{\kappa \mathcal{C}^2} + \frac{\log \mathcal{C}}{\kappa^2 \mathcal{C}}\right], \tag{1}$$

$$\mathcal{P} = \frac{\gamma\,[D-n]}{F_0^2} + \frac{U^2}{2}\left[\frac{1}{\mathcal{N}^2} - \frac{1}{\mathcal{C}^2}\right], \tag{2}$$

where log indicates the natural logarithm, $F_0 = U_0^*/(g D_0^*)^{1/2}$ is the Froude number, $g$ is the gravity acceleration, $\mathcal{N} = \mathcal{C}_{n=D}$, $D$ is the dimensionless depth measured perpendicular to the channel bed, and $\gamma = \cos\alpha$, with $\alpha$ the local bed slope (see Figure 1). The first term on the rhs of (2) is the hydrostatic pressure distribution while the second term is the non-hydrostatic correction induced by the channel curvature. In Dressler's derivation, a resistive term, induced by drag, $\tau_B$, between the flow and bed roughness, is added to the $\mathcal{O}(\sigma^1)$ longitudinal momentum equation computed at $n = 0$, thus a shallow water equation suitable for open channel flows in rivers is obtained:

$$\frac{\partial U}{\partial t} + \frac{U}{\mathcal{N}^2}\frac{\partial U}{\partial s} + \frac{\sin\alpha}{F_0^2} + \Pi + \frac{\tau_B}{D(1-\kappa D/2)} = 0. \tag{3}$$

The first two terms in (3) account for flow acceleration, the third term is due to gravity and the fourth term accounts for the pressure gradient evaluated at the bottom which, from (2), reads

$$\Pi = \left.\frac{\partial \mathcal{P}}{\partial s}\right|_{n=0} = \left(\frac{\gamma}{F_0^2} + \frac{\kappa U^2}{\mathcal{N}^3}\right)\frac{\partial D}{\partial s} - \left(\frac{\kappa \sin\alpha}{F_0^2} - \frac{U^2}{\mathcal{N}^3}\frac{\partial \kappa}{\partial s}\right) D. \tag{4}$$

The last term in Eq. (3), taking into account the drag on the bed, contains a curvature-dependent correction.[31] The Chezy formula $\tau_B = CU^2$ can be assumed, where $C$ is the friction coefficient that is achievable from Einstein's relation[32] as a function of a relative roughness, $d_s = d_s^*/D_0^*$ being $d_s^*$ the mean grain diameter (usually in the range $[10^{-2} - 10^{-4}]$). Finally, the first-order approximation of the kinematic condition at the free surface provides the continuity equation

$$\frac{\partial D}{\partial t} + \frac{U}{\mathcal{N}^2}\frac{\partial D}{\partial s} - V = 0, \tag{5}$$

Downloaded 21 Sep 2012 to 130.192.58.87. Redistribution subject to AIP license or copyright; see http://pof.aip.org/about/rights_and_permissions

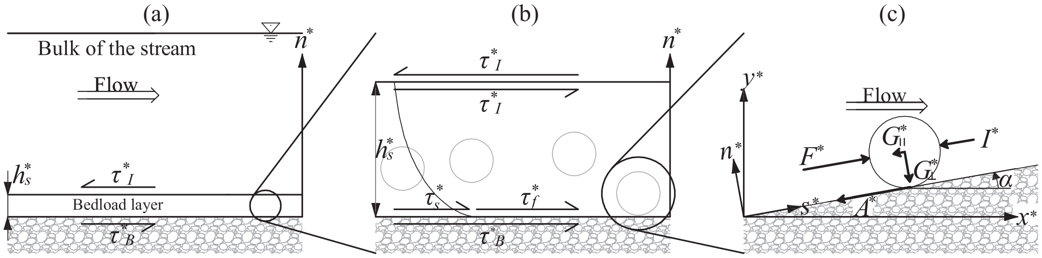

FIG. 2. Scheme of the stresses and forces involved in the bedload layer (see text).

where $V = \mathcal{V}|_{n=D}$. It should be recalled that, for $\kappa \to 0$, Eqs. (3) and (5) reduce to the standard dSV equations, with a flat distribution of the longitudinal velocity, zero normal velocity, and a hydrostatic pressure distribution.

With the aim of proposing a 1D theory for bed forms, the above shallow water hydrodynamic formulation has to be coupled to a morphodynamic model. In order to do so, we consider a mechanistic approach, which extends the formulation by Seminara[29] and Parker,[30] to a non-uniform case. The key point of the mechanistic approach is

$$q = \xi v, \tag{6}$$

where $q = q^*/(Rgd_s^3)^{1/2}$ is the dimensionless sediment transport rate, $\xi = \xi^*/D_0^*(1-p)$ is the areal concentration of the moving particles, $v$ is their dimensionless velocity, $p$ is the bed porosity (set to the usual value[2] $p = 0.4$), $R = \rho_s/\rho - 1$, and $\rho_s$ and $\rho$ are the sediment and fluid densities, respectively (a typical value for silicate sediments[27] is $R = 1.65$).

We neglect the suspended and wash load, so that the overall sediment transport is concentrated in the so-called "bedload layer" ($0 < n < h_s$, see Figure 2(a)), in form of rolling, sliding, and salting. The bedload layer thickness $h_s$ is assumed equal to $2.5d_s$.[29] The hypothesis of considering bedload only allows us to focus our analysis on antidunes. In supercritical flow conditions two competing bedforms can arise: antidunes and cyclic steps.[33] However, a recent experimental study[34] has indicated that antidunes develop when the sediment transport is concentrated on the bedload, differently, cyclic steps arise in the case of prevalent suspended sediment transport.

The concentration and velocity of the moving particles are determined by considering a balance between the forces acting on the sediment particle, the exchange of momentum between the fluid and the particles in the bedload layer, and erosion/deposition processes.

Let us specify the shear stresses involved in the bed load layer. Referring to Figure 2(b), $\tau_I^*$ is defined as the shear stress exerted by the fluid at the interface with the bedload. If the drag force is sufficient to overcome the resistance forces acting on the particles, the total shear stress exerted on the bottom of the bed load layer is split into two components: the (dimensionless) stress exerted by the sediments, $\tau_s$, and the stress exerted by the fluid, $\tau_f$, so that $\tau_I = \tau_s + \tau_f \sim \tau_B$, provided $h_s \ll D$. By imposing a quadratic dependence between $\tau_s$ and the relative velocity of the particle with respect to the fluid, and imposing a standard velocity distribution near the bottom, it is straightforward to obtain the relationship

$$\theta_f = \theta_B - T_\mu \xi \left( \frac{f}{F_0} \sqrt{R d_s \theta_B} - v \right)^2, \tag{7}$$

where $\theta = F_0^2 \tau / R d_s$ is the Shields stress and $f = 11.5$. The coefficient $T_\mu$ is reported in the Appendix together with the coefficients $R_\mu$ and $S_\mu$ that are introduced later on.

According to the standard literature, we can assume that the erosion rate, $\mathcal{E}$, of the particles from the bottom ($n = 0$) is proportional to the fluid shear stress in excess of a threshold quantity $\theta_c$ of incipient mobilization. The deposition rate of the particles on the bottom, $\mathcal{D}$, can instead be assumed to be proportional to the shear stress exerted by the solid, $\tau_s$ (thus decreasing with the increase in $\tau_f$) and the particle concentration. Both the erosion and the deposition are instead inversely proportional

Downloaded 21 Sep 2012 to 130.192.58.87. Redistribution subject to AIP license or copyright; see http://pof.aip.org/about/rights_and_permissions

to the grain diameter. On the basis of experimental and dimensional considerations, Ref. 30 assumes the following relationships:

$$\mathcal{E} = \frac{r_e A_e}{d_s} \left(\theta_f - \theta_c\right)^{3/2}, \tag{8a}$$

$$\mathcal{D} = (1-p)\frac{r_s A_s}{d_s^2}\theta_s^{1/2}\xi, \tag{8b}$$

where $A_e = 0.028$, $A_s = 0.068$, and $r_e$ and $r_s$ are reported in the Appendix. If the erosion and deposition rates do not balance (i.e., non-uniform conditions), the mutual dependence between the spatial change in sediment transport and the temporal change in the bottom elevation can be described—after using (6)—by means of the following equations:

$$\frac{\partial(v\xi)}{\partial x} = \Theta(\mathcal{E} - \mathcal{D}), \tag{9a}$$

$$\frac{\partial \eta}{\partial t} + \frac{\partial(v\xi)}{\partial x} = 0, \tag{9b}$$

where $\Theta = (Rd_s^3)^{1/2}/(1-p)F_0 = \mathcal{O}(10^{-3} - 10^{-4})$. Equation (9a) imposes the sediment balance in the bedload layer, while (9b) is the kinematic condition for the bottom boundary, namely the well-known Exner equation.

Finally, we need a further equation for $v$, which is provided by imposing the dynamical equilibrium of the forces acting on the sediment grain (see Figure 2(c))

$$I^* = F^* - A^* - G_\parallel^*, \tag{10}$$

where $F^*$ is the drag force (proportional to $[f\sqrt{\theta_B} - q]^2$, as in (7)), $A^* = \mu_d G_\perp^*$ is the resistive force due to friction ($\mu_d$ is the dynamical friction coefficient, see the Appendix), $\{G_\perp^*, G_\parallel^*\} = G^*\{\cos\alpha, \sin\alpha\}$ are the normal- and parallel- to the bottom components of the submerged weight of the particles, respectively, and $I^*$ is the particle inertia. In dimensionless form, relation (10) reads

$$\frac{\partial v}{\partial t} + v\frac{\partial v}{\partial x} + R_\mu - S_\mu \left(\frac{f}{F_0}\sqrt{Rd_s\theta_B} - v\right)^2 = 0. \tag{11}$$

It should be noticed that the first two terms in (11), which account for the inertial effects that arise in non-uniform conditions, have remained almost unexplored so far.

Summing up, the complete hydro-morphodynamic model is composed of five PDE Eqs. (3), (5), (9a), (9b), and (11), flanked by three phenomenological relationships (7), (8a), and (8b) for five unknowns: $U$, $D$, $\eta$, $q$, and $\xi$.

## III. STABILITY ANALYSIS AND EXPERIMENTAL VALIDATION

Let us force the flat bed solution of the uniform flow condition, $\eta_0 = -Jx$, with a normal mode perturbation, $\eta_1 = \epsilon \exp(ikx + \Omega t)$ (plus complex conjugate), where $k$ and $\Omega = \Omega_r + i\Omega_i$ are the longitudinal wave number and the complex frequency of the perturbation, respectively, and $\epsilon \ll 1$ is the amplitude of the bed perturbation. Accordingly, the four variables of the morphodynamic model $\mathbf{X} = \{U, D, v, \xi\}$ respond with the following ansatz:

$$\mathbf{X} = \{1, 1, v_0, \xi_0\} + \epsilon \mathbf{X}_1 e^{(ikx + \Omega t)} \quad + \text{c.c}, \tag{12}$$

where $\mathbf{X}_1 = \{u_1, d_1, v_1, \xi_1\}$. As known, $\Omega_r > 0$ ($\Omega_r < 0$) refers to the unstable (stable) conditions, whereas $c = -\Omega_i/k$ is the phase celerity of perturbations. As we are interested in studying the long-term response of the system, and the bed timescales are usually longer than the hydrodynamics timescales, we follow the quasi-steady approximation[4,23] and neglect the time derivatives of all the equations except the Exner equation. The validity of this assumption will be discussed in Sec. V, where we will investigate the effect of the neglected time derivatives on the morphological and free surface instability (i.e., roll waves). After introducing (12) into the above problem, recalling that

Downloaded 21 Sep 2012 to 130.192.58.87. Redistribution subject to AIP license or copyright; see http://pof.aip.org/about/rights_and_permissions

$\partial/\partial s = \gamma\,\partial/\partial x$ and linearizing with respect to $\epsilon$, at the leading order we obtain

$$v_0 = \frac{f\sqrt{J}}{F_0\mathcal{J}} - \sqrt{\frac{R_0}{S_0}\frac{\mu - J}{\mu\mathcal{J}}}, \tag{13}$$

$$\xi_0 = \frac{1}{\rho_0}\left(\frac{J}{Rd_s\mathcal{J}} - \frac{\mu - J}{\mu\mathcal{J}}\theta_{ch}\right), \tag{14}$$

where $\theta_{ch}$ is the critical value for horizontal beds and $\mathcal{J} = \sqrt{1 + J^2}$. $R_0$ and $S_0$ are reported in the Appendix, while $\rho_0$, together with the coefficients $\rho_1$ to $\rho_{10}$, and $\Gamma_5$ and $\Gamma_6$ are reported in the supplementary material.[51] At $\mathcal{O}(\epsilon)$, we instead obtain $\mathcal{A}\mathbf{X}_1 = b$, where

$$\mathcal{A} = \begin{pmatrix} 2J + \mathrm{i}kF_0^2\mathcal{J} & \mathrm{i}k - J + c_D F_0^2\mathcal{J}^2 & 0 & 0 \\ 1 & 1 & 0 & 0 \\ \frac{2J}{F_0^2\mathcal{J}^2} & c_D & -\frac{2\sqrt{J}}{fF_0\mathcal{J}} - \mathrm{i}k\rho_2 & 0 \\ \rho_4 - \frac{\sqrt{J}\rho_6(F_0\rho_7 + f\rho_8)}{F_0\mathcal{J}} & \rho_5 - \frac{c_D F_0\mathcal{J}\rho_6(F_0\rho_7 + f\rho_8)}{2\sqrt{J}} & \frac{\mathrm{i}k\xi_0}{\Theta} + \rho_6\rho_8 & \frac{\mathrm{i}kv_0}{\Theta} + \frac{\rho_9 + \frac{JT_0\rho_8^2}{F_0^2\mathcal{J}^2}}{A_s\Gamma_5 - A_e\Gamma_6} \end{pmatrix},$$

$$b = \begin{pmatrix} -\mathrm{i}k\rho_1 \\ \frac{k^2}{2\mathcal{J}^3} \\ -\mathrm{i}k\rho_3 \\ \rho_{12} \end{pmatrix}, \tag{15}$$

$T_0$ in Eq. (15) is reported in the Appendix and $C_D = \partial C/\partial D|_{D=1}$. After solving the above algebraic system, it is possible to substitute the values of $v_0$, $v_1$, $\xi_0$, and $\xi_1$ in the Exner Eq. (9b) written at the first order

$$\Omega = -\mathrm{i}k\left(\xi_0 v_1 + \xi_1 v_0\right), \tag{16}$$

from which one finally obtains the dispersion relation.

The above problem is basically governed by four dimensionless parameters: $k$, $F_0$, $J$, and $d_s$. By manipulating Einstein's and Chezy's equations at the leading order, the following relationship holds between the Froude number, the slope and the relative roughness

$$F_0\sqrt{\frac{1 + J^2}{J}} + 2.5\log\left(2.5d_s\right) - 6 = 0. \tag{17}$$

Without any loss of generality, we are free to choose three independent parameters: $k$, $F_0$, and $d_s$. By choosing $F_0$ in the range [1, 3] and $d_s = \mathcal{O}(10^{-3})$, it follows $J = \mathcal{O}(10^{-3})$.

The contour plot of the growth factor, $\Omega_r$, as predicted from the above theory, is reported in Figure 3 on the ($k$, $F_0$) plane, for supercritical conditions ($F_0 > 1$) and three different values of the relative roughness, $d_s$ (panels (a)–(c)). In order to validate our theory, we have also reported a set of experimental data, taken from a celebrated benchmark of laboratory analyses on dunes and antidunes, which is reported in Ref. 35. The same dataset has also been adopted to test other analytical models.[23,36] The single experimental values are superimposed onto the ($k$, $F_0$) plane with a marker, where $k$ is the wave number of the antidune that was experimentally observed for a given value of the Froude number, $F_0$.

The comparison appears very satisfactory, since almost all the points from the experiments are enclosed within the marginal stability curve, defined by $\Omega_r = 0$ (thick lines). The model is therefore able to predict the pattern formation correctly. Furthermore, most of the data are very close to the dotted line, which refers to the most unstable wave number versus $F_0$ and corresponds to the pattern selected when the linear theory is used. We also emphasize that the contour plots reported in Figure 3 resemble the results obtained by means of other more sophisticated two-dimensional rotational models.[23,37] Finally, it is worth noticing that the phase velocities of all the cases considered

Downloaded 21 Sep 2012 to 130.192.58.87. Redistribution subject to AIP license or copyright; see http://pof.aip.org/about/rights_and_permissions

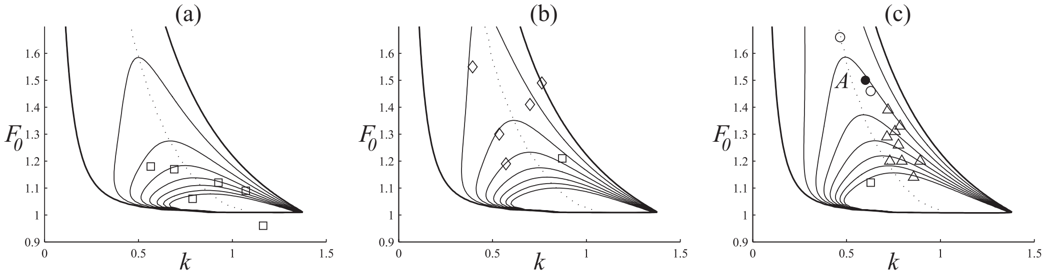

FIG. 3. Comparison between the theoretical results and experimental data. The contour plots show the value of the growth rate: $\Omega_r = 0$ (thick lines), $\Omega_r = [5{-}35] \times 10^{-4}$ (thin lines), and locus of $\max(\Omega_r)$ (dotted lines). The markers refer to the dataset from Ref. 35: run I64 (□ ); run I66 (◯); run I72 (◇); run I74 (△). (a) $d_s = 0.0015$; (b) $d_s = 0.002$; (c) $d_s = 0.0035$.

here are positive, i.e., the perturbation propagate upstream, in agreement with consolidated evidence on rivers under supercritical conditions.

## IV. THE PHYSICAL MECHANISMS THAT DRIVE THE ANTIDUNE INSTABILITY

The response of the sediment transport rate, $q_1$, to the bed perturbation, $\eta_1$, is the key point that can help one to understand the physical mechanisms driving the antidune formation. We recall that $q_1 = \xi_0 v_1 + \xi_1 v_0$ and two components therefore require attention: the particle velocity, $v_1$, and the particle concentration, $\xi_1$. Figures 4(a) and 4(b) show the spatial structure of the $v_1$, $\xi_1$, and $q_1$ responses to an arbitrary bed perturbation. We refer to the $(k, F_0, d_s) = (0.6, 1.5, 3.5 \times 10^{-3})$ case marked by the point $A$ in Figure 3(c), but similar results can be obtained with other values in the instability region. The $k\phi_{q_1}$ phase between the sediment transport rate and bed elevation is also highlighted in Figure 4(b). The $\phi_{q_1}$ angle in fact plays a key role in the development of the bedforms, as it determines whether an infinitesimal perturbation of the bottom grows or decays.[38] In particular, the $0 < \phi_{q_1} < \pi/2$ $(\pi/2 < \phi_{q_1} < \pi)$ range identifies migrating bedforms growing downstream (upstream), while $\pi < \phi_{q_1} < 3\pi/2$ $(3\pi/2 < \phi_{q_1} < 2\pi)$ characterizes migrating bedforms decaying

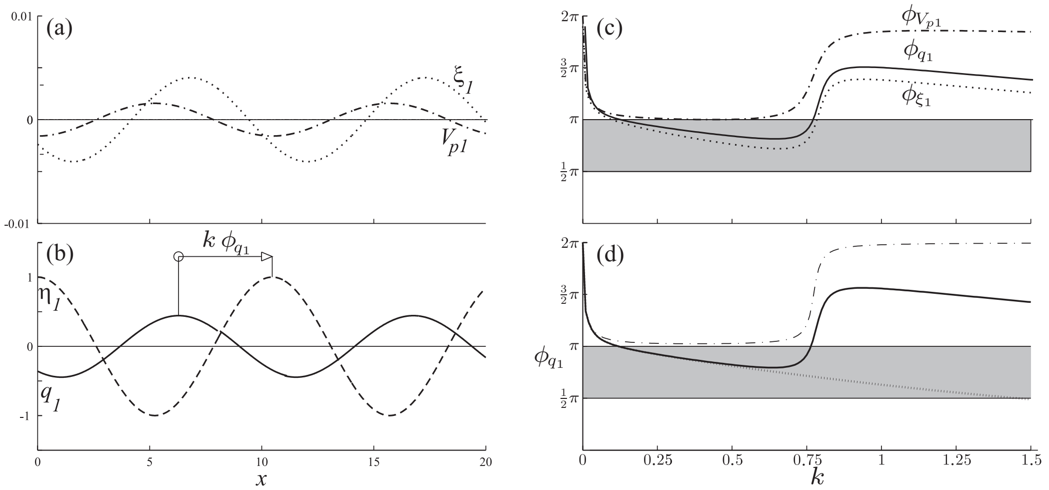

FIG. 4. (a) Perturbation amplitude of $v_1$ (dot-dashed line) and $\xi_1$ (dotted line). (b) Perturbation amplitude of $q_1$ (continuous line) and $\eta_1$ (dashed line); the $k\phi_{q_1}$ phase between sediment transport rate and bed elevation is also shown. (c) Phase angle of $v_1$ (dot-dashed line), $\xi_1$ (dotted), and $q_1$ (continuous line) as a function of the wave number. The gray zone delimits the phase angles corresponding to antidune inception. (d) Phase angle of $q_1$ evaluated as a function of $k$ for three different models: the mechanistic sediment transport model and Dressler equations (continuous line), the mechanistic sediment transport model and dSV equations (dotted line), and the MPM transport model and Dressler equations (dot-dashed line). In all the panels, $d_s = 3.5 \times 10^{-3}$ and $F_0 = 1.5$ (point A in Figure 3(c)); in panels (a) and (b), $k = 0.6$.

Downloaded 21 Sep 2012 to 130.192.58.87. Redistribution subject to AIP license or copyright; see http://pof.aip.org/about/rights_and_permissions

upstream (downstream). Figure 4(c) shows the phase angle of $v_1$, $\xi_1$, and $q_1$ as a function of the wave number.

The phase of the particle concentration $\xi_1$ shows that a wave number interval where $\pi/2 < \phi_{\xi_1} < \pi$ exists in the $k \in [0.1, 0.8]$ range (see the dotted lines in panels (a) and (c)), while the phase angle outside this range is greater than $\pi$. The phase of the particle velocity, $\phi_{v_1}$, instead remains higher than $\pi$ for all the wavenumbers (see the dot-dashed lines in panels (a) and (c)). This means that the sediment transport rate component associated to the particle concentration perturbation, namely $\xi_1 v_0$, is actually responsible for the growth of the instability, while the particle velocity perturbation $v_1$ does not contribute to the generation of the instability. Its role is instead different: since $\phi_{v_1}$ is close to $\pi$ in the instability range dictated by $\phi_{\xi_1}$ (see Fig. 4, panel (c)), the component of $q_1$ due to the particle velocity, $\xi_0 v_1$, drives the upstream migration of the bedforms. However, the remarkable similarity between $\phi_{\xi_1}$ and $\phi_{q_1}$ (compare the continuous and dotted lines in Figures 4(a)–4(c)) confirms that the stabilizing effect of $v_1$ on antidune inception is quite modest.

The mechanistic modeling of the sediment transport therefore reveals that perturbation of the particle concentration is crucial to drive antidune instability. Perturbation of the particle velocity alone is instead unable to trigger instability, but it is responsible for the main contribution to the upstream migration of the bedforms. These features explain why the simplified approaches adopted in previous studies to model the sediment rate hamper the detection of antidune formation in a 1D framework. Such approaches (which do not consider the momentum exchange between the fluid and sediment in the bed load layer) neglect the influence of the particle concentration perturbation. In this way, the sediment transport results only related to the variable $v_1$. Let us consider, for instance, the complex frequency $\Omega$ that corresponds to the widely used MPM formula, which can be obtained by substituting $q = v\xi = 8(\theta - \theta_c)^{3/2}$ in (9b) and inserting the ansatz (12). After linearization, and using the sediment momentum equation at $O(\epsilon)$, we obtain an expression of $\Omega$ which is only related to the particle velocity perturbation $v_1$. In Figure 4(d), the phase angle of $q_1$ (the dot-dashed line) obtained by coupling the Dressler equations with the MPM sediment transport formula is compared with our antidune model. As expected, MPM-like models are not able to predict antidune formation (i.e., $\phi_{q_1} > \pi$ for any $k$) in a 1D framework and a more refined mechanistic sediment transport model is necessary.

A fundamental role in the selection of the antidune wavelength is played by the non-hydrostatic pressure component induced by the curvature of the bottom. This can be demonstrated by eliminating the addenda in Eq. (4) one by one and repeating the stability analysis. This analysis shows that the last term—which is proportional to—is decisive for the wavelength selection. Confirmation of such a feature can be obtained by comparing the stability analysis results deduced using the Dressler equations and the de Saint Venant equations, which only consider the hydrostatic pressure. The differences are evident in the plane $\{k, \phi_{q_1}\}$ shown in Figure 4(d). It should in fact be noticed that the dispersion relation reads $\Omega = -\mathrm{i}kq_1$ and gives the relation between the phase angle of the sediment transport rate and the complex frequency $\Omega$; i.e., $\phi_{q_1} = \arctan[-\Omega_r/\Omega_i]$. It follows that the wavelength selection occurs if $\phi_{q_1}$ exhibits a minimum for a given wave number (since $\Omega_i$ is almost independent from $k$). Figure 4(d) shows that wavelength instability is correctly selected by means of the Dressler model, while the de Saint Venant one predicts the instability (albeit this is due to the mechanistic sediment transport model), but fails to select a wavelength as the corresponding $\phi_{q_1}$ does not exhibit any minimum.

In short, the bed curvature-induced non-hydrostatic pressure component is fundamental to describe the wavelength selection mechanism, while the growth of bedforms and their upstream migration need a sediment transport model that is able to describe non equilibrium conditions.

At this point, it is instructive to evaluate the role of the different forces acting on the single sediment particles (drag, dynamic friction, gravity, and inertia) in determining antidune instability. To this aim, the forces in the equilibrium equation (10) are removed one by one and the corresponding growth rates, celerities, and marginal stability curves are compared. Four different cases are considered (see Table I): case GI (where G stands for gravity and I for inertia) is the complete model, case I (only inertia) does not consider gravity in the particle dynamics, case G (only gravity) neglects particle inertia, and case B (base) only retains the drag force and the dynamical friction.

Downloaded 21 Sep 2012 to 130.192.58.87. Redistribution subject to AIP license or copyright; see http://pof.aip.org/about/rights_and_permissions

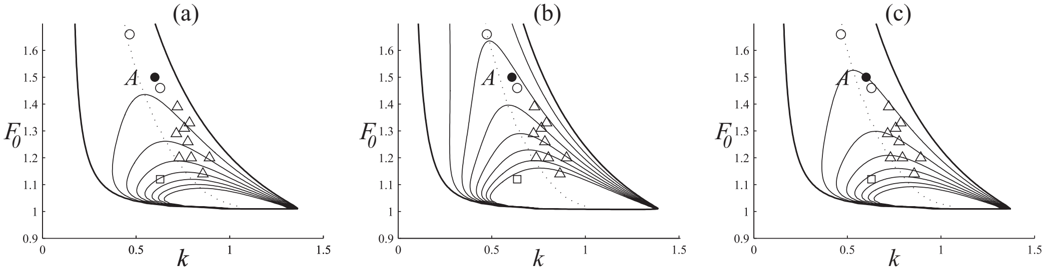

FIG. 5. The growth rate is plotted as a function of $k$ and $F_0$ ($d_s = 3.5 \times 10^{-3}$) for cases G (a), I (b), and B (c) (see Table I). The symbols and lines correspond to those reported in Figure 3.

Figure 5 shows the growth rate, $\Omega_r$, of the perturbation as a function of $k$ and $F_0$ for the I, G, and B cases, while case GI has already been reported in Figure 3(c). In order to make the comparison clearer, the wave numbers, $k_l$ and $k_h$, which delimit the instability interval and the most unstable wave number, $k_{\max}$, are reported in Table I for the representative case of $F_0 = 1.5$. The complex frequency $\Omega$ corresponding to a typical wave number is also given.

The main result that emerges in Figure 5 and Table I is that the marginal stability curves and the most unstable wave numbers do not change significantly if different forces are considered in the dynamic equilibrium of the particle. This general picture therefore suggests that particle inertia and gravity play secondary roles in antidune instability compared to the stream-induced forces. However, a more detailed analysis shows some interesting differences. A comparison between cases G and B reveals that gravity reduces the growth rate. This confirms the results obtained in other works[23] and it is trivial as gravity opposes (favors) uphill (downhill) motion. Upstream sedimentation and downstream erosion processes are accelerated for the same reason and upstream migration celerity is therefore increased.

Particle inertia instead increases the growth rate (see Figures 5(b), 5(c), and Table I). The reason for this behavior becomes clear if one notices that the particle velocity and bed elevation in Figures 4(a) and 4(b) are out of phase and, therefore, the velocity reduces (increases) upstream (downstream) from a bed crest. It follows that inertia works in the opposite direction to gravity and the growth rate of the instability is increased, while the antidune migration celerity is reduced. Unlike from some previous works,[27,39] in which the sediment mass was assumed to be a fundamental ingredient for the inception of antidunes, particle inertia is not crucial in our model for the occurrence of instability and it only gives a (non fundamental) de-stabilizing contribution.

Finally, a comparison of cases B and GI (see Figures 3(c) and 5(c)) highlights that the combined role of gravity and inertia entails an increase in the instability growth rate. This feature can be confirmed from the example reported in Table I, where $\Omega_r$ increases from 0.504 to 1.055, while a small reduction of $\Omega_i$ occurs. Therefore, the de-stabilizing effect due to particle inertia prevails over the stabilizing action caused by gravity. Accordingly, a reduction in the wave celerity with respect to base case B takes place.

TABLE I. Cases with different force balances on the sediment particles. The wavenumbers that delimit the instability zone, $k_l$ and $k_h$, and the most unstable wavenumber, $k_{\max}$, are reported for each case. ($F_0$, $d_s$) = (1.5, 3.5 × $10^{-3}$), while the complex frequency, $\Omega$, is evaluated for $k = 0.6$. The plot corresponding to the considered case is recalled in the last column.

| Case | Forces | $k_l$ | $k_h$ | $k_{\max}$ | $\Omega \times 10^{-3}$ | Figure |
|---|---|---|---|---|---|---|
| GI | $F^*, A^*, G_\parallel^*, I^*$ | 0.121 | 0.763 | 0.528 | 1.055 + 1.431i | 3(c) |
| G | $F^*, A^*, G_\parallel^*$ | 0.186 | 0.717 | 0.514 | 0.345 + 1.649i | 5(a) |
| I | $F^*, A^*, I^*$ | 0.120 | 0.770 | 0.532 | 1.138 + 1.257i | 5(b) |
| B | $F^*, A^*$ | 0.175 | 0.763 | 0.542 | 0.504 + 1.589i | 5(c) |

Downloaded 21 Sep 2012 to 130.192.58.87. Redistribution subject to AIP license or copyright; see http://pof.aip.org/about/rights_and_permissions

## V. FREE SURFACE INSTABILITY

The behavior of our model is investigated in this section, removing the quasi steady assumption introduced in Sec. III. This allows us to confirm its validity for morphodynamic purposes and, at the same time, to study the possible occurrence of free surface instabilities, namely roll waves. To this aim, all the time derivatives in (3), (5), (9b), and (11) are retained and a further viscous dissipative term is introduced into the fluid phase momentum equation. Previous works,[40–43] that investigated free surface stability by means of a shallow water approach, have demonstrated that this dissipative term is in fact fundamental for the description of roll waves. Its role is to suppress free surface instabilities with high wavenumbers, thus confining the free surface instability to a finite region in the wavenumber space. From a physical point of view, this additional term represents the effect of the energy dissipation by shearing normal to the flow.[40] The most frequently used and physically based expression of this term, which has to be added to (3), reads[42]

$$\frac{1}{D Re_e} \frac{\partial}{\partial s} \left( D \frac{\partial U}{\partial s} \right), \tag{18}$$

where $Re_e = U_0^* D_0^* / \nu_e$ and $\nu_e$ represents a suitable eddy viscosity.

If the new system of equations is linearized and the anstaz (12) is introduced, an algebraic system similar to (15) is obtained. By imposing the existence of a non-trivial solution (i.e., $\det \mathcal{A} = 0$) and solving this equation in $\Omega$, the four growth rates associated with the corresponding four solutions can be easily obtained.

We evaluated the stability of the system in the space ($k$, $F_0$) for the same parameters used in Figure 3(c) and found that two modes were always stable, while two modes were unstable over a significant portion of the ($k$, $F_0$) space. The corresponding instability zones are reported in Figure 6, where the gray zone marks the instability zone associated with the free surface perturbation, while the white zone which includes the point A marks the instability zone associated with the bed perturbation.

Comparing Figures 3(c) and 6(a), it can be observed that the morphological instability is practically not affected by the introduction of the additional time derivatives and of the viscous dissipative term. Neither the marginal stability curve nor the locus of max ($\Omega_r$) undergo appreciable changes. By computing the complex frequency associated with the morphodynamic mode for ($k$, $F_0$) = (0.6, 1.5) (point A in Figures 3(c) and 6(a)) we obtain $\Omega = (9.02, 15.20) \times 10^{-4}$. This growth rate is slightly lower than the corresponding quasi steady case GI reported in Table I. This behavior is due to the dissipation term, which reduces the capacity of the flow to transport sediments.

The inclusion of all the time derivatives and the viscous dissipative term allows the presence of roll waves to be detected (Figure 6(a)). The marginal stability curve, the locus of max ($\Omega_r$) and

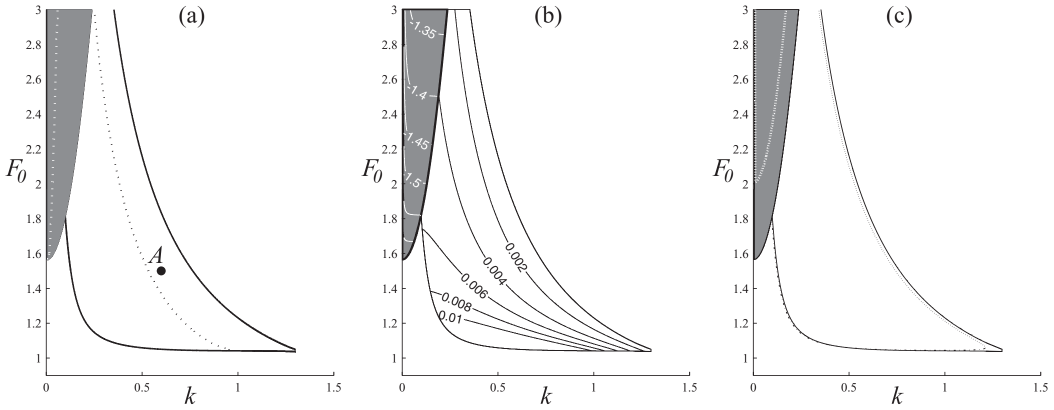

FIG. 6. Panel (a): free surface instability zone (gray) and morphodynamic instability zone (white, indicated with point A); the dotted lines represent the locus of the most amplified wavenumbers. Panel (b): perturbation celerity (it should be recalled that a perturbation with positive celerity migrates upstream). Panel (c): comparison of the instability regions for a friction coefficient dependent (continuous line) and independent (dotted line) on the water depth. All the charts are evaluated for $d_s = 3.5 \times 10^{-3}$ and $Re_e = 10$.

Downloaded 21 Sep 2012 to 130.192.58.87. Redistribution subject to AIP license or copyright; see http://pof.aip.org/about/rights_and_permissions

the perturbation celerity are comparable with the outcomes of other models[43,45] and are coherent with experimental data.[44] The feature of increasing celerity with decreasing Froude number (see Figure 6(b)), observed adopting more refined models,[45] is also captured. It is also interesting to notice that the critical Froude number $F_c$ above which the occurrence of roll waves is possible is about 1.5, apparently in contrast with the well known value $F_c = 2$. However, this behavior is typical of models in which the friction coefficient $C$ used in Chezy's formula is assumed to depend on the water depth.[26,46] If the dependence of $C$ on the water depth is removed—for instance by evaluating $C$ at the uniform state—the classic result $F_c = 2$ is recovered (dotted lines in Figure 6(c)). It should also be noted that the dependence or the lack of dependence of the friction coefficient on $D$ basically has no effect on delimiting the morphological instability region.

A final comment can be made on the choice of the exact value of $Re_e$ adopted for the calculations. A precise estimation of the equivalent eddy viscosity is difficult, as it would require precise knowledge of the flow structure.[43] A common approach to overcome this difficulty is to set $\nu_e$ so that the free surface instability region and the locus of the most amplified wavenumbers fit experimental data. We tried different values for the eddy viscosity, spanning several orders of magnitudes, and observed that although the marginal stability curve is quite sensitive to the actual value of $\nu_e$ (a feature that has also been observed in other works[43]), the locus of the most amplified wavenumbers of the roll waves was influenced much less by this choice.

## VI. THE ABSOLUTE NATURE OF ANTIDUNE INSTABILITY

The convective or absolute nature of instability is a key property. An impulsive perturbation of the equilibrium state produces a convective instability if it migrates because of the basic motion and decays to zero along all the spatiotemporal rays $x/t$. On the contrary, instability is absolute if it increases unbounded throughout the domain.[47,48] Apart from speculative reasons, the nature of antidune instability is also of applicative interest. It is in fact important to evaluate whether antidunes driven by local bed perturbations (e.g., dikes, scours, etc.) only affect the downstream channel or they also spread upstream. This aspect is fundamental to correctly investigate antidune dynamics by numerical simulations and laboratory experiments.

In order to understand the nature of antidune instability, we use the criterion described by Huerre and Monkevitz,[49] who extended the concepts introduced by Briggs[50] and Bers[47] in plasma physics to shear flow instabilities. The response along each ray $x/t$ can be analyzed starting from the saddle point condition

$$\frac{\partial \Omega(k)}{\partial k} = 0, \tag{19}$$

whose complex zero(s) $k_0{=}k_{0r} + \mathrm{i}k_{0i}$ gives the absolute grow rate $\Omega_r(k_0) = \Omega_{0r}$. The theory states that the temporal grow rate along ray $x/t = a$ is given by $\psi(a) = \Omega_{0r}{-}ak_{0i}$. Furthermore, if just real wave numbers are considered, equation $\partial\Omega_r/\partial k = 0$ provides the wave number $k_{\max}$ which gives the maximum temporal grow rate $\Omega_{r,\max} = \Omega_r(k_{\max})$ with the corresponding group velocity $\alpha_{\max} = \partial\Omega/\partial\, k|_{k_{\max}}$.

The criterion states that instability is convective if $\Omega_r(k_{\max}) > 0$ and $\Omega_{0r} < 0$. On the contrary, the flow is absolutely unstable if $\Omega_r(k_{\max}) > 0$ and $\Omega_{0r} > 0$, provided the causality principle is satisfied. Recalling that a spatial branch associated with the grow rate $\tilde{\Omega}_r$ is the locus of complex wave numbers in which $\Omega_r(k_r, k_i) = \tilde{\Omega}_r$, the causality principle requires that the complex $\{k_r, k_i\}$ plane displays the pinching point $k_0$ between two spatial branches $k^+(\Omega_{0r})$ and $k^-(\Omega_{0r})$ of the dispersion

TABLE II. The six pinching points, $k_{0,j}$, and corresponding growth rates, $\Omega_{0,j}$, obtained by introducing the dispersion relation into condition (19), for the $(F_0, d_s) = (1.5, 3.5 \times 10^{-3})$ case.

| Pinching point | 1 | 2 | 3 | 4 | 5 | 6 |
|---|---|---|---|---|---|---|
| $k_{0,j}$ | −0.464 − 0.078i | 0.464 − 0.078i | 2.023i | −1.434i | 0.036i | 5.890i |
| $\Omega_{0,j} \times 10^{-3}$ | 1.020 + 1.8364i | 1.020 + 1.8364i | 2054.676 | 6.333 | −0.582 | −4502.531 |

Downloaded 21 Sep 2012 to 130.192.58.87. Redistribution subject to AIP license or copyright; see http://pof.aip.org/about/rights_and_permissions

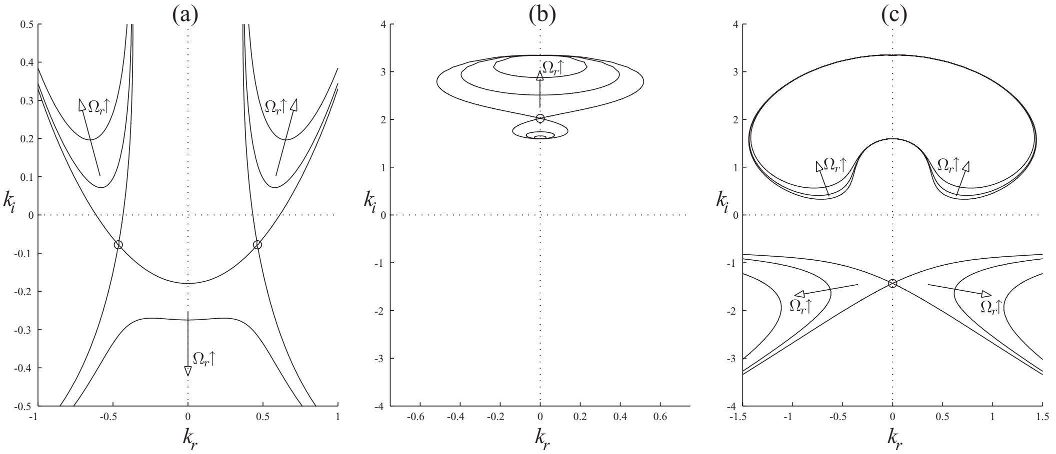

FIG. 7. Behaviour of the spatial branches in the $\{k_r, k_i\}$ plane at pinching points $k_{0,1}$ and $k_{0,2}$ (a), $k_{0,3}$ (b), and $k_{0,4}$ in the $(F_0, d_s) = (1.5, 3.5 \times 10^{-3})$ case. The $j$th pinching point is marked by a circle in each panel. The arrows indicate in which direction the spatial branches move as $\Omega_r$ attains large values. The spatial branches evaluated for $\Omega_r = 1.5\ \Omega_{0r,j}$ (first inner line) and for $\Omega_r = \Omega_{0r,j}$ (second inner line) are also reported in order to clarify this aspect.

relation, and that the spatial branches are well confined within their respective $k_i$ half-planes when $\Omega_r \gg \Omega_{0r}$.

Introducing the previously obtained dispersion relation into condition (19) yields a sixth-order polynomial. In the exemplifying case $(F_0, d_s) = (1.5, 3.5 \times 10^{-3})$, the complex wave numbers $k_{0,j}$ $(j = 1, \ldots, 6)$ which give the vanishing group velocity and the corresponding grow rates $\Omega_{0r,j} = \Omega_r(k_{0,j})$ are reported in Table II (where it can be seen that different parameter values do not change the final results of the present analysis). It can be observed that $k_{0,5}$ and $k_{0,6}$ have $\Omega_{0r,j} < 0$ and would therefore lead to a convective instability, while the other four solutions have $\Omega_{0r,j} > 0$: $k_{0,1}$ and $k_{0,2}$ are complex conjugate, while $k_{0,3}$ and $k_{0,4}$ are purely imaginary.

In order to asses the nature of the instability, the behavior of the spatial branches that merge at the $j$th branch points, in which $\Omega_{0r,j} > 0$, has to be checked. At least two of the spatial branches diverging from at least one branching point must lie on distinct $k_i$ half-plane as $\Omega_r$ attains large values[49] for the instability to be absolute. The behavior of the spatial branches for the pinching points $k_{0,1}$ and $k_{0,2}$ is shown in Figure 7(a). One observes that, for increasing $\Omega_r$ (notice the trend indicated by the arrows), two of the three branches which merge at the pinching points are in the upper $k_i$ half plane, while one is in the lower one. This indicates the absolute nature of the antidune instability.

Figures 7(b) and 7(c) refer to pinching points $k_{0,3}$ and $k_{0,4}$, respectively. As for increasing $\Omega_r$, the two branches merging at the pinching points remain in the same $k_i$ half-plane (in the upper one for $k_{0,3}$ and in the lower one for $k_{0,4}$), but the behavior of these pinching points does not contribute to the determination of the absolute nature of antidune instability.

## VII. CONCLUSIONS

In this paper, we have proposed a 1D model to describe the morphological instability of a granular bed bounding a turbulent supercritical open-channel flow. The very good matching between the theoretical results and the experimental data demonstrates that a suitable one-dimensional model is sufficient to catch the features of antidune instability. The key points of the model are (1) the mechanistic modelling of the sediment transport, which considers the particle concentration and particle velocity separately, and (2) the Dressler equations, which are able to take into account the impact of the channel bottom curvature on the stream dynamics.

A careful analysis of the model components has elucidated the crucial role played by three key physical mechanisms. First, the instability is driven by the phase shift between the bed perturbation

Downloaded 21 Sep 2012 to 130.192.58.87. Redistribution subject to AIP license or copyright; see http://pof.aip.org/about/rights_and_permissions

and the perturbation of the sediment concentration. Second, the phase shift between bed perturbation and particle velocity perturbation instead controls the upstream migration of antidunes. Finally, the non-hydrostatic pressure correction induced by the channel bottom curvature is essential for wavelength selection. The importance of the first two mechanisms explains why the commonly used sediment transport formulas based on equilibrium (e.g., the Meyer-Peter-Müeller formula) are unable to describe the antidune inception in a 1D framework. In the same way, simplified 1D fluid dynamic models that assume hydrostatic pressure fail to select the right wavelength.

Furthermore, we have investigated the role of gravity and inertia on sediment dynamics. As in previous studies, we have demonstrated that gravity reduces antidune instability while inertia promotes it. However, both of them play a secondary role in the occurrence of instability compared to stream-induced drag and dynamic friction. We stress that our model predicts antidune formation by taking only bedload into account (coherently with the experimental evidence).

We have obtained the dispersion relation in closed form. This result paves the way toward interesting new studies (e.g., non-modal analysis) that would be precluded, or much more cumbersome, in 2D or 3D frameworks. An important example of such studies is given in this work, in which we have demonstrated the absolute nature of antidune instability, a result that can help in the interpretation of laboratory and numerical experiments on antidunes.

In this paper, we have focused on stream-bed instability for the case of supercritical open-channel flows. However, we also tested whether our model was able to describe the dune inception characteristic of subcritical streams. However, as expected, the 1D model is unable to detect any instability. This failure is due to the fact that dunes are roughly out of phase with the free surface and, therefore, the stream tends to accelerate (slow down) on the crests (troughs) inducing an increase (decrease) in sediment transport. It follows that the global geometry of the stream-bed system tends to contrast the dune inception and, for this reason, 2D and 3D models are necessary to catch the subtle destabilizing mechanisms that drive dune instability.

## APPENDIX: PARAMETERS OF THE MECHANISTIC SEDIMENT TRANSPORT MODEL

### 1. Parameters in flat bed conditions

$$R_0 = \frac{R\mu_{d0}}{F_0^2(R+1)}, \quad S_0 = \frac{4\mu_{d0}(3\lambda^2\theta_{ch}f^2)^{-1}}{c_s d_s(R+1)}, \quad T_0 = \frac{F_0^2\mu_{d0}(1-p)}{\lambda^2\theta_{ch}f^2 d_s^2 R}, \tag{A1}$$

where $c_s = 4/3$, $\lambda = 0.7$, $\theta_{ch} = 0.047$, $p = 0.4$ and for silicate sediments $R = 1.65$.

### 2. Correction coefficients to account for gravity

$$r_{sc} = \cos\alpha\left(1+\frac{\tan\alpha}{\mu}\right), \quad r_\mu = 1+\frac{\tan\alpha}{\mu}-\frac{\tan\alpha}{\mu_{d0}}, \quad r_{dc} = \cos\alpha\left(1+\frac{\tan\alpha}{\mu_d}\right), \tag{A2}$$

$$r_e = \left[1+(1-r_\mu r_{dc})K_0\right]^{-3/2}, \quad r_s = (r_\mu r_{dc})^{-1/2}, \quad r_\lambda = \left(\frac{r_{sc}}{r_{dc}}\right)^{1/2}, \tag{A3}$$

$$\mu_d = \mu_{d0} r_\mu, \quad R_\mu = R_0 r_\mu r_{dc}, \quad S_\mu = S_0\frac{r_\mu}{r_\lambda^2}, \quad T_\mu = T_0\frac{r_\mu}{r_\lambda^2}, \quad \theta_c = \theta_{ch} r_{sc}, \tag{A4}$$

where $\mu_{d0} = 0.3$ and $\mu = 0.6$.

[1] G. Seminara, "Fluvial sedimentary patterns," Annu. Rev. Fluid Mech. **42**, 43–66 (2010).

[2] C. Camporeale and L. Ridolfi, "Nonnormality and transient behavior of the de Saint Venant Exner equations," Water Resour. Res. **45**, W08418–W08418, doi:10.1029/2008WR007587 (2009).

[3] C. Camporeale and L. Ridolfi, "Modal versus nonmodal linear stability analysis of river dunes," Phys. Fluids **23**, 104102 (2011).

Downloaded 21 Sep 2012 to 130.192.58.87. Redistribution subject to AIP license or copyright; see http://pof.aip.org/about/rights_and_permissions

[4] B. Federici and G. Seminara, "On the convective nature of bar instability," J. Fluid Mech. **487**, 125–145 (2003).

[5] C. Camporeale and L. Ridolfi, "Convective nature of the planimetric instability in meandering river dynamics," Phys. Rev. E **73**, 026311 (2006).

[6] O. Devauchelle, L. Malverti, É. Lajeunesse, P. Y. Lagree, C. Josserand, and K. D. Nguyen Thu-Lam, "Stability of bedforms in laminar flows with free surface: From bars to ripples," J. Fluid Mech. **642**, 329–348 (2010).

[7] M. Colombini and A. Stocchino, "Three-dimensional river bed forms," J. Fluid Mech. **695**, 1–18 (2012).

[8] J. W. Lillycrop, J. D. Rosati, and D. D. McGehee, "A study on sand waves in the Panama City, Florida, entrance channel," Technical Report CERC-TR-89-7, US Army Engineer and Development Center, 1989.

[9] M. Gao and D. Roelvink, "Pilot study on navigation channel regulation works in the north channel, Yangtze estuary," in *Proceedings of 32nd Conference on Coastal Engineering, Shanghai* (Coastal Engineering Research Council, 2010), pp. 1–13.

[10] M. L. Amsler, H. H. Prendes, M. D. Montagnini, R. Szupiany, and M. H. Garcia, "Prediction of dune height in sand-bed rivers: The case of the Paraná River, Argentina," in *Proceedings of the 3rd IAHR Symposium on River, Coastal and Estuarine Morphodynamics* (IAHR Secret, Madrid, 2003), pp. 1104–1113.

[11] J. Shaw and R. Kellerhals, "Paleohydraulic interpretation of antidune bedforms with applications to antidunes in gravel," J. Sediment. Petrol. **47**, 57266 (1977).

[12] B. Rust and V. Gostin, "Fossil transverse ribs in holocene alluvial fan deposits, Depot Creek, South Australia," J. Sediment. Petrol. **51**, 441–444 (1981).

[13] C. R. Fielding, "Upper flow regime sheets, lenses and scour fills: Extending the range of architectural elements for fluvial sediment bodies," Sedim. Geol. **190**, 227–240 (2006).

[14] J. B. Jones and P. J. Mulholland, *Streams and Groundwaters*, 1st ed. (Elsevier, New York, 2000).

[15] D. Corenblit, A. C. Baas, G. Bornette, J. Darrozes, S. Delmotte, R. A. Francis, A. M. Gurnell, F. Julien, R. J. Naiman, and J. Steiger, "Feedbacks between geomorphology and biota controlling earth surface processes and landforms: A review of foundation concepts and current understandings," Earth-Sci. Rev. **106**, 307–331 (2011).

[16] L. Bardini, F. Boano, M. B. Cardenas, R. Revelli, and L. Ridolfi, "Nutrient cycling in bedform induced hyporheic zones," Geochim. Cosmochim. Acta **84**, 47–61 (2012).

[17] J. F. Kennedy, "The mechanics of dunes and antidunes in erodible-bed channels," J. Fluid Mech. **16**, 521–544 (1963).

[18] A. J. Reynolds, "Waves on an erodible bed," J. Fluid Mech. **22**, 113–133 (1965).

[19] T. Hayashi, "Formation of dunes and antidunes in open channels," J. Hydr. Div. **96**(2), 357–366 (1970).

[20] S. E. Coleman and J. D. Fenton, "Potential-flow instability theory and alluvial stream bed forms," J. Fluid Mech. **418**, 101–117 (2000).

[21] F. Engelund, "Instability of erodible beds," J. Fluid Mech. **42**, 225–244 (1970).

[22] J. Fredsøe, "On the development of dunes in erodible channels," J. Fluid Mech. **64**, 1–16 (1974).

[23] M. Colombini, "Revisiting the linear theory of sand dunes," J. Fluid Mech. **502**, 1–16 (2004).

[24] P. J. Schmid and D. S. Henningson, *Stability and Transition in Shear Flows*, 1st ed. (Springer, 2001).

[25] P. Huerre, and M. Rossi, "Hydrodynamic instabilities in open flows," in *Hydrodynamic and Instabilities*, edited by C. Goldreche and P. Manneville (Cambridge University Press, Cambridge, 2000), pp. 159–229.

[26] M. H. Gradowczyk, "Wave propagation and boundary instability in erodible-bed channels," J. Fluid Mech. **33**, 93–112 (1970).

[27] C. DiCristo, M. Iervolino, and A. Vacca, "Linear stability analysis of a 1-D model with dynamical description of bed-load transport," J. Hydraul. Res. **44**, 480–487 (2006).

[28] R. F. Dressler, "New nonlinear shallow-flow equations with curvature," J. Hydraul. Res. **16**, 205–222 (1978).

[29] G. Seminara, L. Solari, and G. Parker, "Bed load at low shields stress on arbitrarily sloping beds: Failure of the Bagnold hypothesis," Water Resour. Res. **38**, 1249, doi:10.1029/2001WR000681 (2002).

[30] G. Parker, G. Seminara, and L. Solari, "Bed load at low shields stress on arbitrarily sloping beds: Alternative entrainment formulation," Water Resour. Res. **39**, 1183, doi:10.1029/2001WR001253 (2003).

[31] R. F. Dressler and V. Yevjevich, "Hydraulic resistance terms modified for the Dressler curved flow equations," J. Hydraul. Res. **22**, 145–156 (1978).

[32] H. A. Einstein, "The bed-load function for sediment transport in open channels flows," Technical Report No. 1026, U.S. Department of Agriculture, 1950.

[33] S. Kostic, O. Sequeiros, B. Spinewine, and G. Parker, "Cyclic steps: A phenomenon of supercritical shallow flow from the high mountains to the bottom of the ocean," J. Hydro-Environ. Res. **3**, 167–172 (2010).

[34] M. Yokokawa, Y. Takahashi, H. Yamamura, Y. Kishima, G. Parker, and N. Izumi, "Antidunes and cyclic steps: Relating their features to a suspension index and a velocity coefficient," in *Japan Geoscience Union Meeting 2011* (Japan Geoscience Union, 2011), pp. SCG064–14.

[35] H. P. Guy, D. B. Simons, and E. V. Richardson, "Summary of alluvial channel data from flume experiments," U.S. Geol. Surv. Prof. Pap. **462-I**, 1–96 (1966).

[36] M. Colombini and A. Stocchino, "Finite amplitude river dunes," J. Fluid Mech. **611**, 283–306 (2008).

[37] C. Camporeale, C. Canuto, and L. Ridolfi, "A spectral approach for the stability analysis of turbulent open-channel flows over granular beds," Theor. Comput. Fluid Dyn. **26**, 51–80 (2012).

[38] T. J. Hanratty, "Stability of surfaces that are dissolving or being formed by convective diffusion," Annu. Rev. Fluid Mech. **13**, 231–252 (1981).

[39] G. Parker, "Sediment inertia as cause of river antidunes," J. Hydr. Div. **101**, 211–221 (1975).

[40] D. J. Needham and J. H. Merkin, "On roll waves down an open inclined channel," Proc. R. Soc. London **394**, 259–278 (1984).

[41] S. H. Hwang and H. C. Chang, "Turbulent and inertial roll waves in inclined film flow," Phys. Fluids **30**, 12591268 (1987).

[42] N. J. Balmforth and S. Mandre, "Dynamics of roll waves," J. Fluid Mech. **514**, 1–33 (2004).

Downloaded 21 Sep 2012 to 130.192.58.87. Redistribution subject to AIP license or copyright; see http://pof.aip.org/about/rights_and_permissions

[43] N. J. Balmforth and A. Vakil, "Cyclic steps and roll waves in shallow water over an erodible bed," J. Fluid Mech. **695**, 35–62 (2012).
[44] R. R. Brock, "Development of roll-wave trains in open channels," J. Hydr. Div. **95**, 1401–1427 (1969).
[45] M. Colombini and A. Stocchino, "Coupling or decoupling bed and flow dynamics: Fast and slow sediment waves at high froude numbers," Phys. Fluids **17**, 036602 (2005).
[46] P. Luchini and F. Charru, "The phase lead of shear stress in shallow-water flow over a perturbed bottom," J. Fluid Mech. **665**, 516–539 (2010).
[47] A. Bers, "Space-time evolution of plasma instabilities: absolute and convective," in *Handbook of Plasma Physics*, edited by M. Rosenbluth and R. Sagdeev (North Holland, Amsterdam, 1983), pp. 159–229.
[48] P. Huerre, "Open shear flow instabilities," in *Perspectives in Fluid Dynamics: A Collective Introduction to Current Research*, edited by H. J. K. Batchelor and M. Worster (Cambridge University Press, Cambridge, 2000), pp. 159–229.
[49] P. Huerre and P. A. Monkevitz, "Local and global instabilities in spatially developing flows," Annu. Rev. Fluid Mech. **22**, 473–537 (1990).
[50] R. J. Briggs, *Electron-Stream Interaction with Plasma* (MIT, Boston, 1964).
[51] See supplementary material at http://dx.doi.org/10.1063/1.4753943 for the value of $\rho_0$, together with the coefficients $\rho_1$ to $\rho_{10}$, and $\Gamma_5$ and $\Gamma_6$.

Downloaded 21 Sep 2012 to 130.192.58.87. Redistribution subject to AIP license or copyright; see http://pof.aip.org/about/rights_and_permissions